The Astrophysical Journal Letters, 907:L15 (9pp), 2021 January 20 https://doi.org/10.3847/2041-8213/abd3aa

ALMA Survey of Orion Planck Galactic Cold Clumps (ALMASOP): Detection of Extremely High-density Compact Structure of Prestellar Cores and Multiple Substructures Within

Dipen Sahu[1], Sheng-Yuan Liu[1], Tie Liu[2], Neal J. Evans II[3], Naomi Hirano[1], Ken'ichi Tatematsu[4,29], Chin-Fei Lee[1], Kee-Tae Kim[5,6], Somnath Dutta[1], Dana Alina[7], Leonardo Bronfman[8], Maria Cunningham[9], David J. Eden[10], Guido Garay[8], Paul F. Goldsmith[11], Jinhua He[8,12,13], Shih-Ying Hsu[1,14], Kai-Syun Jhan[1,14], Doug Johnstone[15,16], Mika Juvela[17], Gwanjeong Kim[4], Yi-Jehng Kuan[1,18], Woojin Kwon[19], Chang Won Lee[5,6], Jeong-Eun Lee[20], Di Li[21,22], Pak Shing Li[23], Shanghuo Li[5], Qiu-Yi Luo[2], Julien Montillaud[24], Anthony Moraghan[1], Veli-Matti Pelkonen[25], Sheng-Li Qin[26], Isabelle Ristorcelli[27], Patricio Sanhueza[28,29], Hsien Shang[1], Zhi-Qiang Shen[2], Archana Soam[30], Yuefang Wu[31], Qizhou Zhang[32], and Jianjun Zhou[33]

[1] Academia Sinica Institute of Astronomy and Astrophysics, 11F of AS/NTU Astronomy-Mathematics Building, No.1, Sec. 4, Roosevelt Road, Taipei 10617, Taiwan R.O.C.; dsahu@asiaa.sinica.edu.tw, syliu@asiaa.sinica.edu.tw
[2] Shanghai Astronomical Observatory, Chinese Academy of Sciences, 80 Nandan Road, Shanghai 200030, People's Republic of China; liutie@shao.ac.cn
[3] Department of Astronomy The University of Texas at Austin 2515 Speedway, Stop C1400 Austin, TX 78712-1205, USA
[4] Nobeyama Radio Observatory, National Astronomical Observatory of Japan, National Institutes of Natural Sciences, 462-2 Nobeyama, Minamimaki, Minamisaku, Nagano 384-1305, Japan
[5] Korea Astronomy and Space Science Institute, 776 Daedeokdae-ro, Yuseong-gu, Daejeon 34055, Republic of Korea
[6] University of Science and Technology, Korea (UST), 217 Gajeong-ro, Yuseong-gu, Daejeon 34113, Republic of Korea
[7] Department of Physics, School of Sciences and Humanities, Nazarbayev University, Nur-Sultan 010000, Kazakhstan
[8] Departamento de Astronomía, Universidad de Chile, Camino el Observatorio 1515, Las Condes, Santiago, Chile
[9] School of Physics, University of New South Wales(UNSW), Sydney, NSW 2052, Australia
[10] Astrophysics Research Institute, Liverpool John Moores University, iC2, Liverpool Science Park, 146 Brownlow Hill, Liverpool, L3 5RF, UK
[11] Jet Propulsion Laboratory, California Institute of Technology, 4800 Oak Grove Drive, Pasadena, CA 91109, USA
[12] Yunnan Observatories, Chinese Academy of Sciences, 396 Yangfangwang, Guandu District, Kunming, 650216, People's Republic of China
[13] Chinese Academy of Sciences South America Center for Astronomy, National Astronomical Observatories, CAS, Beijing 100101, People's Republic of China
[14] National Taiwan University (NTU), Taiwan R.O.C.
[15] NRC Herzberg Astronomy and Astrophysics, 5071 West Saanich Road, Victoria, BC, V9E 2E7, Canada
[16] Department of Physics and Astronomy, University of Victoria, Victoria, BC, V8P 5C2, Canada
[17] Department of Physics, P.O. Box 64, FI-00014, University of Helsinki, Finland
[18] Department of Earth Sciences, National Taiwan Normal University, Taipei, Taiwan R.O.C.
[19] Department of Earth Science Education, Seoul National University, 1 Gwanak-ro, Gwanak-gu, Seoul 08826, Republic of Korea
[20] School of Space Research, Kyung Hee University, 1732, Deogyeong-Daero, Giheung-gu Yongin-shi, Gyunggi-do 17104, Republic of Korea
[21] National Astronomical Observatories, Chinese Academy of Sciences, Beijing 100101, People's Republic of China
[22] NAOC-UKZN Computational Astrophysics Centre, University of KwaZulu-Natal, Durban 4000, South Africa
[23] Department of Astronomy, University of California, Berkeley, CA 94720, USA
[24] Institut UTINAM—UMR 6213—CNRS–Univ. Bourgogne Franche Comté, OSU THETA, 41bis avenue de l'Observatoire, F-25000 Besançon, France
[25] Institut de Ciències del Cosmos, Universitat de Barcelona, IEEC-UB, Martí i Franqués 1, E-08028 Barcelona, Spain
[26] Department of Astronomy, Yunnan University, and Key Laboratory of Particle Astrophysics of Yunnan Province, Kunming, 650091, People's Republic of China
[27] Université de Toulouse, UPS-OMP, IRAP, F-31028 Toulouse cedex 4, France
[28] National Astronomical Observatory of Japan, National Institutes of Natural Sciences, 2-21-1 Osawa, Mitaka, Tokyo 181-8588, Japan
[29] Department of Astronomical Science, SOKENDAI (The Graduate University for Advanced Studies), 2-21-1 Osawa, Mitaka, Tokyo 181-8588, Japan
[30] SOFIA Science Center, Universities Space Research Association, NASA Ames Research Center, Moffett Field, California 94035, USA
[31] Department of Astronomy, Peking University, 100871 Beijing, People's Republic of China
[32] Center for Astrophysics | Harvard & Smithsonian, 60 Garden Street, Cambridge, MA 02138, USA
[33] Xinjiang Astronomical Observatory, CAS: Urumqi, Xinjiang, CN, People's Republic of China
Received 2020 November 23; revised 2020 December 15; accepted 2020 December 15; published 2021 January 19

Abstract

Prestellar cores are self-gravitating dense and cold structures within molecular clouds where future stars are born. They are expected, at the stage of transitioning to the protostellar phase, to harbor centrally concentrated dense (sub)structures that will seed the formation of a new star or the binary/multiple stellar systems. Characterizing this critical stage of evolution is key to our understanding of star formation. In this work, we report the detection of high-density (sub)structures on the thousand-astronomical-unit (au) scale in a sample of dense prestellar cores. Through our recent ALMA observations toward the Orion Planck Galactic Cold Clumps, we have found five extremely dense prestellar cores, which have centrally concentrated regions of ∼2000 au in size, and several 10^7 cm^{-3} in average density. Masses of these centrally dense regions are in the range of 0.30 to 6.89 $M_\odot$. For the first time, our higher resolution observations (0.8″ ∼ 320 au) further reveal that one of the cores shows clear signatures of fragmentation; such individual substructures/fragments have sizes of 800–1700 au, masses of 0.08 to 0.84 $M_\odot$, densities of $2-8\times10^7$ cm^{-3}, and separations of ∼1200 au. The substructures are massive enough ($\gtrsim$0.1 $M_\odot$) to form young stellar objects and are likely examples of the earliest stage of stellar embryos that can lead to widely (∼1200 au) separated multiple systems.

Unified Astronomy Thesaurus concepts: Molecular clouds (1072); Collapsing clouds (267); Star forming regions (1565); Star formation (1569); Protostars (1302)

1. Introduction

Stars form from the gravitational collapse of dense molecular cloud cores in the interstellar medium. Characterization of the dense cores is therefore of great importance for gaining insights into the initial conditions and evolutionary stages in star formation. Starless cores, which are condensations of matter without any embedded young stellar objects (YSOs), are considered as the earliest phase of star formation. A subset of the starless cores, called prestellar cores, are gravitationally bound and will presumably collapse to form YSOs (André et al. 2014). The evolution of prestellar cores to YSOs, and whether they form single or multiple stellar systems, however, is far from being understood.

While extensive efforts have been made previously to investigate the physical and chemical properties of starless and prestellar cores with single element telescopes (e.g., Caselli 2011), the densest and presumably innermost 1000 au of such cores are yet to be characterized due to the limited angular, hence spatial, resolution. This scale is, however, crucial for testing theories of fragmentation to form multiple systems.

To this end, survey observations of starless cores in nearby molecular clouds (including, for example, Perseus, Ophiuchus, and Chamaeleon) with modern (sub)millimeter interferometers, such as the Combined Array for Research in Millimeter-wave Astronomy (CARMA), the Submillimeter Array (SMA), and the Atacama Large Millimeter and submillimeter Array (ALMA) were conducted (e.g., Schnee et al. 2010, 2012; Dunham et al. 2016; Kirk et al. 2017). In these survey observations, very few localized sources were recovered because of the insensitivity of interferometers to small fluctuations in extended emission. Among those detected sources, some turned out to be protostellar, while others remained starless with no additional substructure in their (sub) millimeter continuum emission. Such results suggest that the density profiles of starless cores are predominantly flat, consistent with the earlier suggestions (e.g., Ward-Thompson et al. 1994, 1999; Shirley et al. 2000; Caselli et al. 2019). A profile having nearly constant density at small radii (∼few 1000 au) is reminiscent of the "flat zone" in Bonnor–Ebert spheres (Ebert 1955; Bonnor 1956).

Meanwhile, observations indicate that the multiplicity fraction and the companion star fraction are highest in Class 0 protostars and decrease in more evolved protostars (Chen et al. 2013; Tobin et al. 2016). This implies that multiple systems may develop at an even earlier phase. Indeed, some theoretical works suggest that substructures in prestellar cores can be produced by turbulent fragmentation at a scale of 1000 au, which will form wide-multiple stellar systems (Offner et al. 2010), and these should be visible using sensitive interferometers (Offner et al. 2012). However, none of the observational surveys described in the previous paragraph found secondary/multiple substructures within dense cores at a scale of 1000 au. Although a few studies report cases of substructure and fragmentation in specific starless cores (e.g., Kirk et al. 2009; Chen & Arce 2010; Nakamura et al. 2012; Takahashi et al. 2013; Friesen et al. 2014; Pineda et al. 2015; Ohashi et al. 2018; Tatematsu et al. 2020) they are associated with high-density condensation, and not related to the substructures (1000 au scale) in the central dense region of prestellar cores.

In a recent ALMA survey, Tokuda et al. (2020) reported the presence of very low mass ($\sim 10^{-2}\,M_{\odot}$, $n_{\rm H_2} \sim 10^5\,{\rm cm}^{-3}$) substructure toward starless cores at a scale of 1000 au; these substructures are not massive enough to produce multiple stars. In another observational effort to study the inner dense region of the prestellar core L1544 (Caselli et al. 2019), no substructures were detected inside the central dense region ($\sim$2000 au with $n_{\rm H_2} \geqslant 10^6{\rm cm}^{-3}$) of the core, where stellar multiplets are expected to potentially develop.

Recently, we performed a survey (ALMA Survey of Orion Planck Galactic Cold Clumps or ALMASOP; Dutta et al. 2020) with ALMA, in which we targeted 72 cores toward the Orion Molecular Clouds (distance ∼400 pc; Kounkel et al. 2018). An overview of the ALMASOP is presented in Dutta et al. (2020). Among the 72 targets in ALMASOP observations, 23 were previously classified as (candidate) starless cores. While all these starless cores were detected in the SCUBA-2 observations (with a core scale of ∼0.1 pc or 20000 au), only 16 of them are detected by the ALMASOP ACA observations (scale ∼0.03 pc or 6000 au). In this Letter, we highlight the detection of a central compact dense structure toward a sample of five cores and the discovery of substructures within one of them using the ALMA 12-m array.

2. Observations

The observations of ALMASOP (project ID:2018.1.00302. S.; PI: Tie Liu) were carried out with ALMA in Cycle 6 toward 72 fields during 2018 October to 2019 January. The observations were executed in four blocks in three different array configurations: 12 m C43-5 (TM1), 12 m C43-2 (TM2), and 7 m ACA, resulting in a resolution ranging 0.″34–5.″5 in the 1.3 mm band. The correlator was configured into four spectral windows with 1.875 GHz bandwidth, which provides a spectral resolution of 1.129 MHz, corresponding to velocity resolutions between 1.465 and 1.563 km s^{-1}. We adopted this coarse velocity resolution to facilitate efficient continuum observations and to maximize the spectral line coverage. The spectral setup covers the continuum emission at 233.0 GHz and 216.6 GHz, and offers simultaneous coverage of the molecular lines CO (2–1), $C^{18}O$ (2–1), N_2D^+ (3–2), SiO (5–4), and other hot corino tracers as well (see Hsu et al. 2020). The remaining details of the observational parameters are presented in Dutta et al. (2020).

The calibrated visibility data were obtained using CASA 5.4 (Common Astronomy Software Applications package; McMullin et al. 2007) pipeline script as delivered by the observatory. The visibility data for different configurations and executions corresponding to the 72 sources were then separated into continuum and spectral data, and imaged jointly. The 1.3 mm continuum images of the sources are generated through CASA's tclean task with the "automask" on, the hogbom deconvolver, and a robust weighting of 0.5.

3. Results

3.1. Detection of Compact Dense Structure inside Prestellar Cores

We present in Figures 1 and 2(c) the detection of the 1.3 mm (dust) continuum emission in color toward the five targets (G208.68-19.20N2, G209.29-19.65S1, G209.94-19.52N, G212.10-19.15N1, and G205.46-14.46M3 (G205-M3 hereafter))

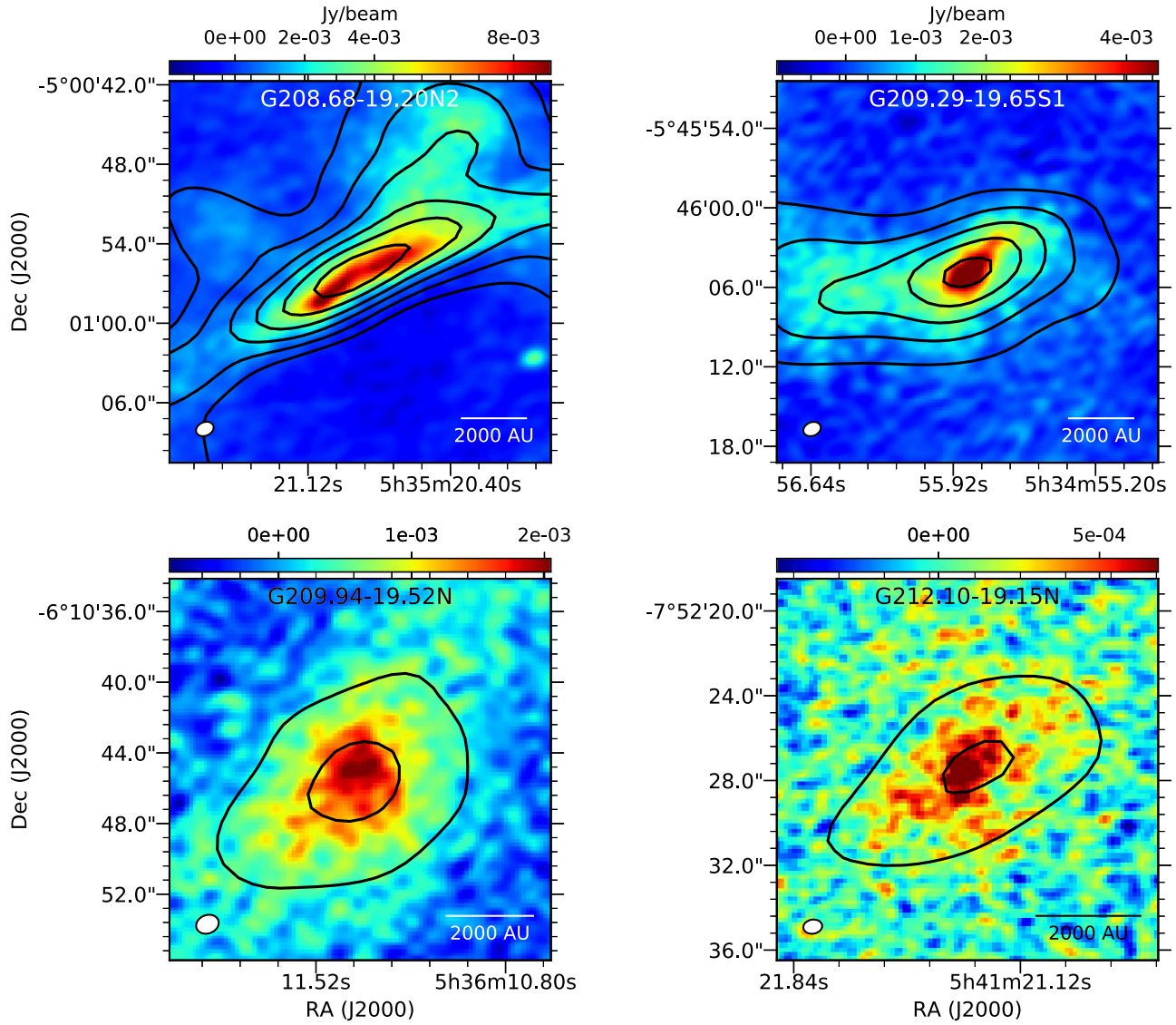

Figure 1. The central dense region of the prestellar cores G208.68-19.20N2 (top left), G209.29-19.65S1 (top right), G209.94-19.52N (bottom left), and G212.10-19.15N1 (bottom right). The contours represent the 1.3 mm continuum observed by the ACA with levels 5, 10, 15σ..., where $\sigma = 3.4$, 1.9, 2.5, 1.6 mJy beam^{-1}, respectively, for the sources; and the color scales show the ALMA ACA+TM2 detection of the centrally dense region. Beam sizes (typically 1.2″) for each source are shown in the lower left of each panel.

with the ALMA ACA+TM2 configurations at a resolution of ∼1.″2. As introduced in Section 1, 16 of the 23 candidate starless cores were detected by the ACA observations at a resolution of ∼6″ and the five targets are among the 16 cores. Compared with the other 11 detections, the five cores discussed in this paper have further compact dense features within the structures seen by the ACA. However, their dust emission is not like the YSOs, which have point-like compact emission features as imaged using ALMA-TM1 configuration (∼0.″3).

None of the five cores displays an outflow signature when observed in CO ($J = 2$-1), its isotopologue lines and SiO ($J = 5$-4) (Dutta et al. 2020). Neither near-infrared nor mid-infrared emission is present within these targets based on our archival search.[34] Meanwhile, toward the central region of these five cores, CO appears fully depleted while N_2D^+ traces well the 1.3 mm (dust) continuum (see Figure 3). This is in accordance with their intense N_2D^+ emission and high $[N_2D^+]/[N_2H^+]$ abundance ratio of ⩾0.1 seen by the NRO 45 m telescope at a larger (∼0.05 pc to 0.1 pc) scale (Kim et al. 2020). All these lines of evidence suggest that the five cores are genuinely chemically evolved prestellar cores. Note that all of these sources were earlier classified as "starless" by Yi et al. (2018), although Kirk et al. (2016) using JCMT survey results classified G205-M3 as YSO because of the presence of a YSO (Megeath et al. 2012; Stutz et al. 2013) within the very extended (∼65″) envelope surrounding the core. The nearest YSO is ∼27″ away from the position of G205-M3 core (see Figure 2, panel 1), and therefore not directly associated.

The flux density of the observed structure toward each of the five cores can be estimated from two-dimensional (2D) Gaussian fitting. We have neither gas nor dust temperature measurements on the observed angular scales. Nevertheless, given their prestellar nature, we assume the temperature of the compact component is at most 10 K and can go as low as 6.5 K (Crapsi et al. 2007; Keto & Caselli 2010). By adopting a (dust) specific absorption coefficient (per mass, with a gas-to-dust

[34] (https://irsa.ipac.caltech.edu/irsaviewer/)

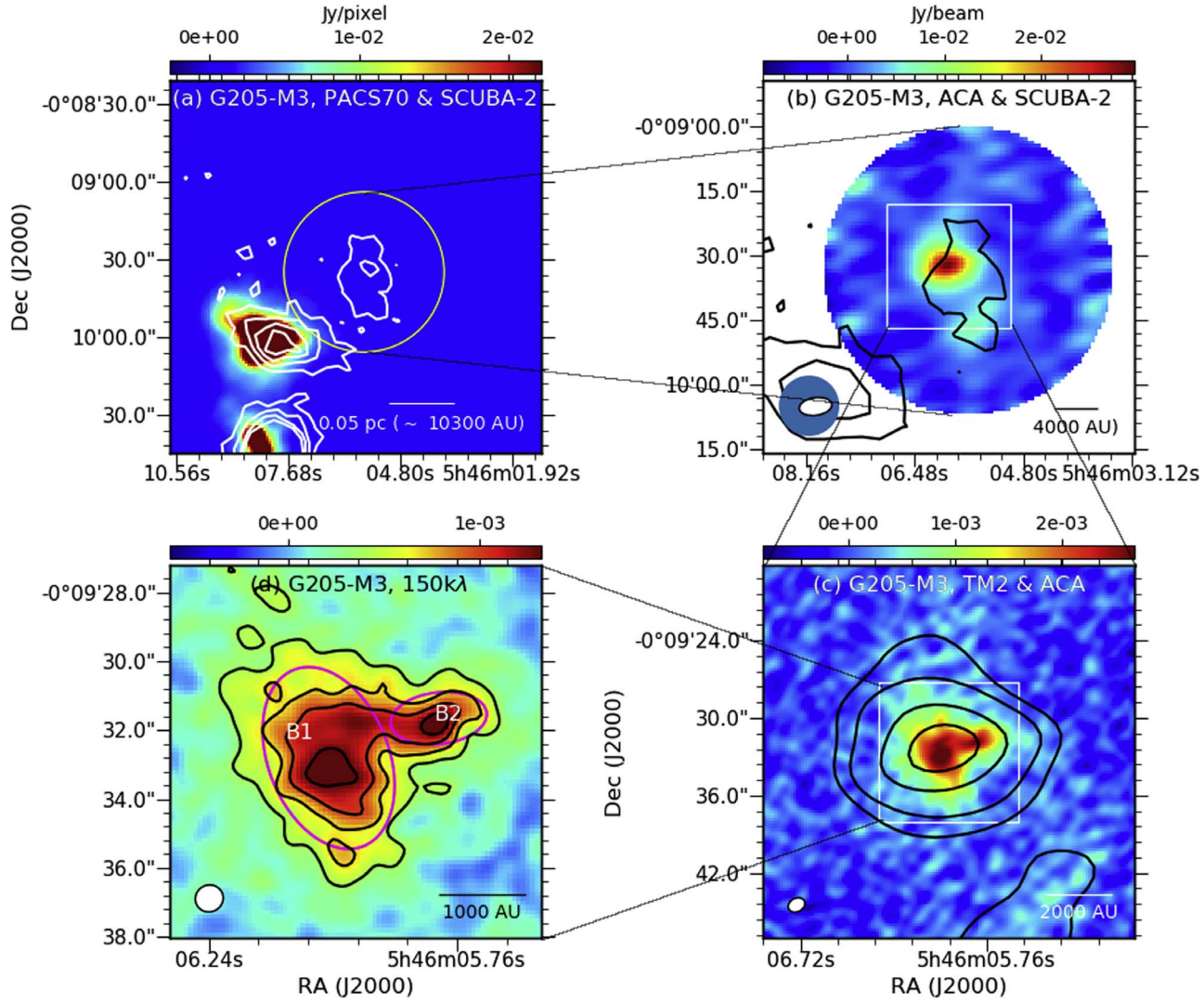

Figure 2. The structure of G205.46-14.56M3 as revealed at different wavelengths and scales. Panel (a) shows 0.85 mm continuum observed by SCUBA-2 in contours 0.3, 0.5, 0.7, 0.9× peak (where peak = 671.4 mJy beam^{-1} corresponds to the peak flux of closest protostellar core) overplotted on the 70 μm mid-infrared image taken by Herschel PACS. Panel (b) shows the SCUBA-2 850 μm continuum in contours (6σ, σ = 38 mJy beam^{-1}) and the ACA 1.3 mm continuum map in color. Both beams are shown in left bottom corner. Panel(c) shows the highly dense central region as revealed by the ALMA ACA+TM2 dust continuum map (synthesized beam $\sim$ 1.2″). Plotted in contours are the ACA continuum with levels 3, 5, 10, 15σ…, where σ = 1.6 mJy beam^{-1}. Panel (d) zooms toward the central region at a higher resolution (synthesized beam 0.8″) where the substructures (B1 and B2) are visible. The contours are at 4, 6, 10 and 13σ levels where σ = 0.1 mJy beam^{-1}. The ellipses correspond to the FWHM sizes inferred from the two-component Gaussian fitting.

mass ratio of 100) $\kappa = 0.009\,\mathrm{cm^2\,g^{-1}}$ at the observing wavelength for grains with thick icy mantles after 10^5 yr of coagulation (Ossenkopf & Henning 1994), we infer the source masses. The effective radius of the cores ($R_{\rm core}$) is estimated as $\sqrt{(\mathrm{major} \times \mathrm{minor})}/2$, where "major" and "minor" correspond to the two axes of the ellipse obtained from the 2D Gaussian fitting, and the gas column density can be found as $N_{\rm H_2} = M/(\pi \mu_{\rm H_2}\, m_{\rm H} R_{\rm core}^2)$. By assuming a spherical geometry, the gas volume density can also be calculated from $n_{\rm H_2} = 3M/(4\pi \mu_{\rm H_2}\, m_{\rm H} R_{\rm core}^3)$, where $\mu_{\rm H_2}$ (=2.8) is the molecular weight per hydrogen molecule (Kauffmann et al. 2008), and $m_{\rm H}$ is the proton mass. The mass, size, column density, and volume density of the cores inferred from both the ACA observations and the ACA+TM2 observations are presented in Table 1.

3.2. Substructures in the Prestellar Core G205-M3

G205-M3 is the only core where we detect substructures at a scale of 1000 au inside the compact dense structure of the core (also see Section 4.1.1). We show in Figure 2 the (dust) continuum images of the G205-M3 core. Different *uv*–tapering of the visibility data has been employed to highlight the intricate features of the core seen at different angular scales. The G205-M3 core size in SCUBA-2 observation (beam size $\sim$ 14″) is on the order of 0.05 pc or 10000 au (Yi et al. 2018). The core is detected by ACA (beam $\sim$ 6″, see Figure 2(b)) with an overall size on the order of 4000 au and, moreover, the faint substructure can be readily discerned. At a higher (1.″2) resolution (see Figure 2(c)) an asymmetric structure can be seen with an average core size of $\sim$2000 au.

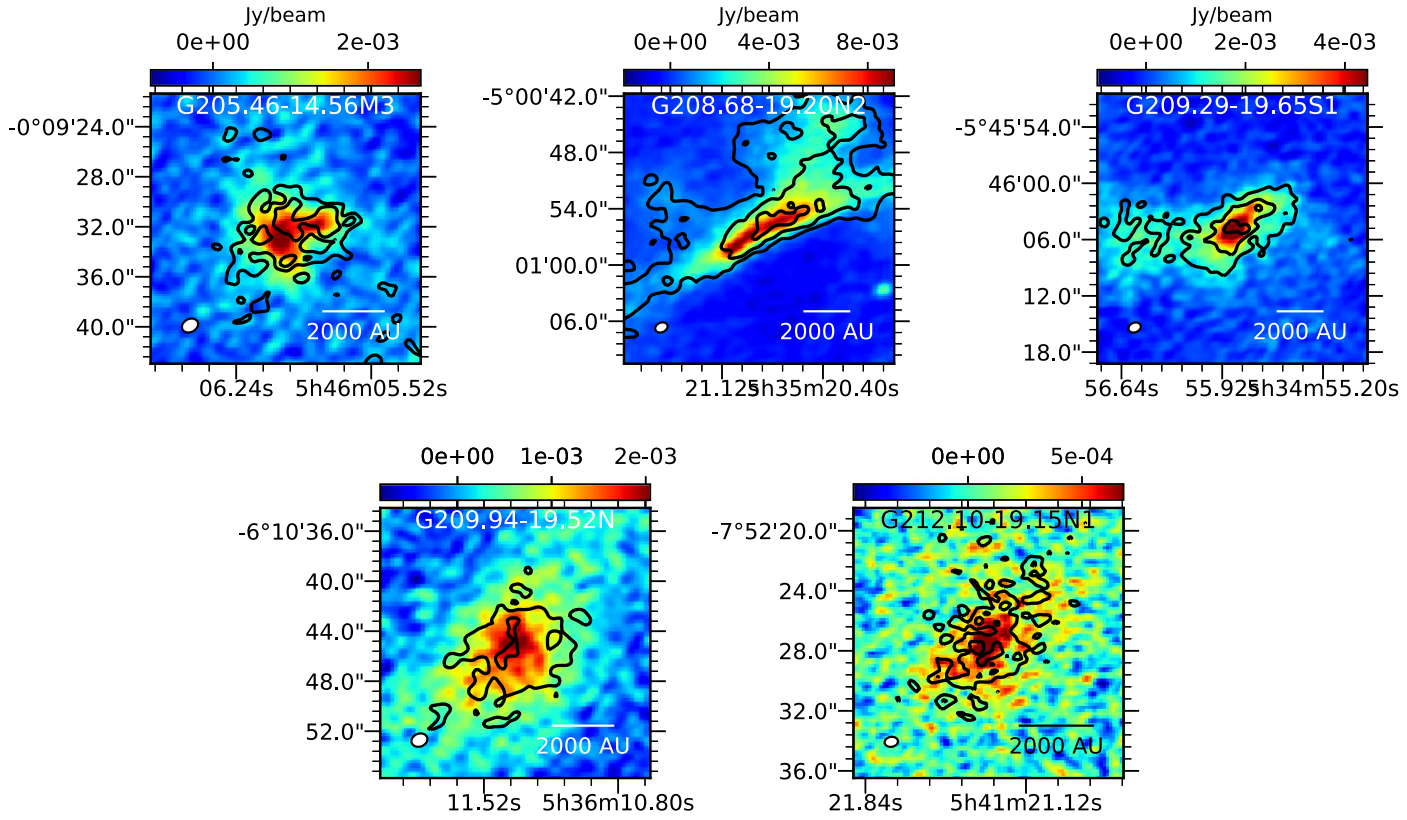

Figure 3. Integrated N_2D^+ emission in contours overplotted on the ALMA ACA+TM2 dust continuum map. The contours are 3σ, 5σ, 7σ…, where σ (rms) = 20 and 17 mJy beam^{-1} km s^{-1}for G205.46-14.56M3 and G212.10-19.15N1, respectively. For G208.68-19.20N2, G209.29-19.65S1, and G209.94-19.52N the rms (σ) = 32, 20, 21 mJy beam^{-1} km s^{-1}, respectively, and contours are 5, 10, 15σ.

Further zooming into the source with an angular resolution of 0.″8 (corresponding to a uv-taper of 150 kλ; Figure 2(d)), the inner 2000 au region of G205-M3 is then resolved into two noticeable substructures. These substructures are named B1 and B2 (see Figure 2(d)). These substructures were also identified using a dendrogram analysis, see Figure 4. They were fitted simultaneously with 2D Gaussian fitting. The two components are, respectively, $5.''5 \times 3.''5$ and $2.''8 \times 1.''5$ in size and separated roughly by 1200 au (3″). The masses of B1 and B2 are 0.38–0.84 $M_\odot$ and 0.08–0.19 $M_\odot$, respectively, if a (dust) temperature range of 6.5–10 K is assumed, with larger masses associated with the lower temperatures. Their corresponding volume densities, considering a spherical geometry, are listed in Table 1.

4. Discussion

Summarizing the results, a series of observations of increasingly better resolution and sensitivity has revealed increasingly compact, denser structures in a small subset of starless cores. In this section, we discuss the physical properties, the stability, and the dynamical state of these structures.

4.1. Detection of Compact Structures

In the ACA/ALMA maps, the flux densities of G205-M3 enclosed in apertures with an equivalent radius r of 0.″4, 1.″1, 2.″2, 5.″7, and 14.″9 centered at the peak position of B1 are 1.4 mJy, 7.5 mJy, 24.8 mJy, 52.2 mJy, and 99.5 mJy respectively. Assuming the gas temperature and dust property are uniform within these scales, we find the corresponding enclosed masses will scale as $r^{1.2}$, which hints at a density profile of $r^{-1.8}$ between 300 au and 10000 au scale. Using a similar method, for other cores (except G208-N2) the masses scale as $r^{1.2} - r^{1.3}$, and therefore their density profiles vary as $r^{-1.7} - r^{-1.8}$. The actual density profile could be even steeper if the dust temperature decreases toward the center of the core. These structures are thus not consistent with Bonnor–Ebert spheres unless the inner region of constant density is very small (Dunham et al. 2016). Such systems are generally very close to the initiation of collapse or they have begun to collapse. Based on their statistical analysis on the lifetime of starless cores, Dunham et al. (2016) and also Kirk et al. (2017) argued that only evolved cores with short lifetime ($\sim 10^4$ year) can be detected by interferometers. Therefore, the five cores detected at high resolution ($\sim$1.″2) likely represent an evolved starless stage, just before the onset of star formation.

Such dense regions can be compared with the well known prestellar core "kernel" in L1544 (Caselli et al. 2019). The average and peak densities of the five prestellar cores are at least 10 times higher than that of the L1544 core, although the sizes of the regions are comparable.

4.1.1. Search for Substructures at 1000 au Scale

Do the five cores have substructures inside the compact dense regions? We use different methods, e.g., uv-tapering of the image, slicing along possible substructure features to identify the intensity variation, and the dendrogram technique. This helps us identify the real and prominent substructures that are not related to imaging artifacts (e.g., Caselli et al. 2019) and weak substructure features. Prominent signatures of

Table 1
ALMA-ACA and ACA+TM2 Configuration 1.3 mm Continuum Results of Five Presetellar Cores

Source	R.A. (J2000)	Decl. (J2000)	FWHM ($''$)	S_ν(1.3 mm) (mJy)	$M_{\rm gas}$ ($M_\odot$)	n_{H2} (cm^{-3})	N_{H2} (cm^{-2})	Diameter (au)	L_J[b] (au)	α (FWHM)[c] $-$(km s^{-1})
					ACA results					
G205.46–14.56M3[a]	05:46:05.99	−00:09:32.37	8.4 × 7.0	79.8	0.76–1.69	$6.4-14.2\times10^{6}$	$1.9-4.3\times10^{23}$	3067	1561	0.68 (0.40)
G208.68–19.20N2	05:35:20.72	−05:00:54.09	26.7 × 7.7	724.0	6.93–15.36	$8.9-19.7\times10^{6}$	$5.1-11.3\times10^{23}$	5735	1325	0.17 (0.49)
G209.29–19.65S1	05:34:56.04	−05:46:05.28	21.5 × 7.5	266.0	2.55–5.64	$4.7-10.4\times10^{6}$	$2.4-5.4\times10^{23}$	5087	1826	1.12 (0.97)
G209.94–19.52N	05:36:11.39	−06:10:45.93	14.2 × 7.2	129.1	1.24–2.74	$4.5-9.9\times10^{6}$	$1.8-4.0\times10^{23}$	4059	1868	0.83 (0.57)
G212.10–19.15N1	05:41:21.27	−07:52:27.01	11.6 × 6.0	47.1	0.45–1.00	$2.9-6.5\times10^{6}$	$1.0-2.2\times10^{23}$	3337	2306	1.80 (0.55)
					Combined ACA+TM2 results					
G205.46-14.56M3[a]	05:46:05.96	−00:09:32.45	6.0 × 4.8	53.2	0.51–1.13	$1.2-2.8\times10^{7}$	$2.7-5.9\times10^{23}$	2146	1119	0.71 (0.40)
G208.68-19.20N2	05:35:20.76	−05:00:55.21	16.3 × 3.6	325.0	3.11-6.89	$2.6-5.7\times10^{7}$	$7.9-17.0\times10^{23}$	3087	781	0.21 (0.49)
G209.29–19.65S1	05:34:55.84	−05:46:04.81	7.8 × 3.9	98.6	0.94–2.09	$2.1-4.7\times10^{7}$	$4.7-10.0\times10^{23}$	2205	856	1.32 (0.97)
G209.94–19.52N	05:36:11.38	−06:10:45.65	10.7 × 6.5	89.3	0.86–1.89	$0.6-1.2\times10^{7}$	$1.8-4.1\times10^{23}$	3344	1680	0.99 (0.57)
G212.10–19.15N1	05:41:21.28	−07:52:27.50	7.7 × 4.2	31.8	0.30–0.67	$0.6-1.4\times10^{7}$	$1.4-3.2\times10^{23}$	2264	1568	1.83 (0.55)
					Substructure in G205-M3					
B1	05:46:06.008	−00.09.32.812	5.5 × 3.5	39.4	0.38-0.84	$1.9-4.2\times10^{7}$	$3.22-7.14\times10^{23}$	1755	1014	0.79 (0.40)
B2	05:46:05.795	−00.09.31.659	2.8 × 1.5	8.8	0.08–0.19	$3.7-8.2\times10^{7}$	$3.03-6.71\times10^{23}$	820	730	1.76 (0.40)

Notes. R.A. and decl. correspond to the peak positions of 2D Gaussian fitting. The range for $M_{\rm gas}$, n_{H2}, N_{H2} corresponds to the estimation, assuming T_K=10 K and 6.5 K respectively.
[a] The source name in the JCMT survey (Yi et al. 2018) is G205.46-14.56N1.
[b] Jeans lengths (L_J) calculated at 10 K; at 6.5 K the values will be lower.
[c] Virial parameters calculated at 10 K with FWHMs obtained by Kim et al. (2020); at 6.5 K the values will be lower; see Section 4.3 for details.

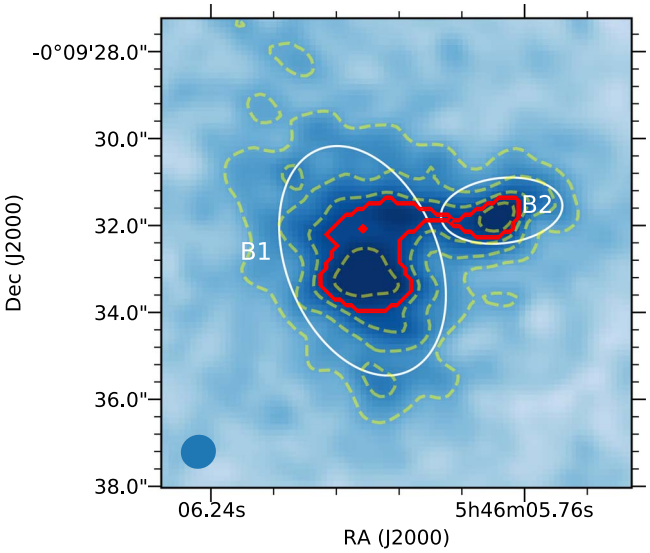

Figure 4. The red contours show the condensations/blobs as identified using dendrogram analysis. White ellipses correspond to FWHM size of the two component Gaussian fitting of the condensations B1 and B2. Dotted contours correspond to 1.3 mm dust continuum at 0.8″ resolution with the levels 4σ, 7σ, 10σ, and 13σ where the rms noise is given by $\sigma = 0.1$ mJy beam^{-1}.

substructures are found only toward G205-M3 (Section 3.2). Among the other four cores, the G208-N2 core appears elongated and similar to a filamentary structure (more details of this core will be presented by Hirano et al. 2021, in preparation). However, the intensity fluctuations along the apparent substructures are at most comparable to the noise level, therefore we see no evident signs of substructure toward G208-N2. Similarly, we do not find substructures toward the other remaining cores, and their detailed physical evolutionary status and density structure will be described in a future work (Sahu et al. 2021, in preparation).

4.2. Thermal Stability

Assuming first an isothermal molecular core, being supported only by its thermal pressure against gravity without considering nonthermal gas motions, one can estimate the Jeans length scale beyond which gravitational collapse would prevail. The Jeans length is defined by: $L_J = \sqrt{\frac{\pi C_s^2}{G\rho_0}}$, where G is the gravitational constant, ρ_0 is mass density, and C_s is the isothermal sound speed, $C_s = (k_B T/\mu_p m_H)^{0.5}$, with $\mu_p = 2.37$ (Kauffmann et al. 2008). Yi et al. (2018) found that at the scale of the SCUBA-2 observation, these five cores are unstable based on the Jeans analysis. We find similar results for the dense structures seen at the ACA (6″) and TM2 (∼1.2″ scales; see Table 1). The dense structures in the five cores have sizes significantly greater than their corresponding Jeans lengths, implying that they are Jeans unstable.

The adopted gas temperature is a major uncertainty in the above analysis. While we have adopted a gas temperature of 10 K for all sources, Kim et al. (2020) found from N_2H^+ and N_2D^+ line observations that under LTE conditions the gas temperatures of the five cores are in the range of 10.8–17.3 K at larger scales with an average density (∼10^5 cm^{-3}). Nevertheless, the cores remain unstable even if we adopt a gas temperature of 20 K. In fact, the temperatures of the central compact dense regions are likely to be lower than 10 K given their high density. A good example is L1544, for which Caselli et al. (2019) assumed a core temperature to be 6.5 K for its high density (∼10^6 cm^{-3}). The average density of the central dense regions in our core sample is at least 10 times higher than L1544 and a gas temperature of 6.5 K is therefore viable. At this temperature all the core structures detected by ACA are Jeans unstable, further highlighting their prestellar nature.

4.3. Dynamical State

We particularly focus on the dynamical state toward the G205-M3 core, where substructures are detected. To assess the dynamical state of the regions, we use molecular line data to determine thermal and nonthermal contributions, using $\sigma_v^2 = \sigma_{th}^2 + \sigma_{nt}^2$, where $\sigma_{th} = (k_B T/m)^{0.5}$, where m is the mass of the observed molecule, and σ_{nt} are the thermal and nonthermal components, respectively. The nonthermal contributions could include infall, rotation, and streaming motions, but they are usually attributed to turbulence. Ideally, we would use the line data on the scales of the substructures, but our velocity resolution is insufficient. We instead consider information from NH_3 with an FWHM linewidth (Δv) of 0.88 km s^{-1} (Cesaroni & Wilson 1994) on a scale of 40 arcseconds (2×10^4 au) and from N_2D^+ with $\Delta v = 0.4$ km s^{-1}on a scale of 8000 au. Using $\Delta v = (8ln2)^{0.5}\sigma_v$, we obtain $\sigma_v = 0.37$ km s^{-1}for NH_3 and 0.17 km s^{-1}for N_2D^+. If we assume $T_K = 10$ K, $\sigma_{th} = 0.068$ km s^{-1}for NH_3, and 0.053 km s^{-1}for N_2D^+, resulting in $\sigma_{nt} = 0.37$ km s^{-1}for NH_3 or $\sigma_{nt} = 0.16$ for N_2D^+, with the smaller value more likely relevant to the individual cores and indicating nearly equal contributions from turbulence and thermal broadening. The isothermal sound speed, C_s is 0.19 km s^{-1}at $T_K = 10$ K, indicating that the turbulence is supersonic, with a Mach number of 2 based on NH_3 or transonic, with Mach number of 0.8 based on N_2D^+. Taken at face value, these results suggest that the turbulence has decayed on small scales. The effective sound speed, $c_{s,eff} = (C_s^2 + \sigma_{nt}^2)^{0.5}$, is 0.247 km s^{-1}, using the data from N_2D^+.

The fate of the substructures can be assessed from their virial parameters. The parameter $\alpha_{vir} = 2aE_k/|E_g|$, where E_k is the kinetic energy and E_g is the gravitational potential energy, and $a = 2 \pm 1$ for a wide range of geometries and density structures (Kauffmann et al. 2013). The virial parameter can be written as $\alpha_{vir} = 5.6 \times 10^{-3} a c_{s,eff}^2 R(\text{au}) M(M_\odot)^{-1}$. Taking the sizes and masses and the effective sound speed of 0.247 km s^{-1}, we obtain $\alpha_{vir} = 0.36a$ to $0.79a$ for B1 and $\alpha_{vir} = 0.74a$ to $1.76a$ for B2. This calculation suggests that the substructures are close to being gravitationally bound, even if the nonthermal component is entirely due to turbulence. Other motions, such as infall, may be present. It is at least plausible that the substructures are collapsing to form separate objects. Using similar calculations, we found that the four other dense cores are also close to being gravitationally bound (see Table 1). This again supports the evolved prestellar nature of the cores.

4.4. Substructures toward G205-M3 and Stellar Multiplicity

We have detected, for the first time, substructures within the central compact dense region (∼2000 au) of the prestellar core G205-M3. What will be the fate of these kinds of substructures?

If the substructures are in freefall, they are likely to form separate objects that could be members of a wide binary. They are unlikely to coalesce before they collapse. The minimum

time to coalesce is the crossing time. Using the projected separation of 1148 au (also see the Appendix) and the effective sound speed of 0.247 km s^{-1}, we calculate $t_{\rm cross} = 5.0\ {\rm yr}\ c_{\rm s,eff}^{-1} = 2.3 \times 10^4$ yr, where s is the projected separation in astronomical units and $c_{\rm s,eff}$ is in km s^{-1}. This estimate assumes that there is no separation along the line of sight and that they are headed on a collision course. In contrast, the freefall time is $\sqrt{3\pi/32\rho_0 G}$ (where $\rho_0 = n_{H_2}\mu_{H_2}m_H$ with $\mu_{H_2} = 2.8$), for a minimum H_2 number density (n_{H_2}) of 1.9×10^7cm^{-3}, $t_{\rm ff} < 7.06 \times 10^3$ yr, which is much shorter than t_{cross}. On the other hand, a binary system will be bound if the internal energy: $E_{int} = 1/2\mu v^2 - Gm_1m_2/r < 0$, where μ is the reduced mass of the two bodies. Considering the mass of B1 and B2 substructures/subcores, the system will be bound for a velocity difference (v) of 0.8–1.2 km s^{-1}. From the low resolution spectral data (N_2D^+), we find that the velocity difference is at most 1.465 km s^{-1}. Therefore, it is very plausible that the subcores may eventually form a wide binary system. Notably, Karnath et al. (2020) reported substructures associated with protostellar candidates. Those substructures appear to trace an early stage of protostellar evolution, during which substructures are associated with collapsing fragments and individual components may be optically thick hydrostatic cores. The detected structures toward the prestellar core (G205-M3) are therefore not some transient features; they likely persist into the protostellar phase as well.

4.5. Physical Explanations for Fragmentations

In the "gravoturbulent fragmentation" (Palau et al. 2018) scenario fragmentation takes place in a self-gravitating turbulent medium. In this case, the density is determined by enhancements created by turbulence (e.g., Padoan & Nordlund 2002; Fisher 2004; Goodwin et al. 2004; Offner et al. 2010). Based on this theory, Offner et al. (2012) predicted that prestellar core fragmentation can be observable at the 1000 au scale. It is plausible that fragmentation toward the G205-M3 core represents such a case. However, the nondetections of subcores in other prestellar cores possibly imply a younger stage than the G205-M3 core, and they may fragment in a later period of their evolution.

5. Summary

We present 1.3 mm dust continuum observations using different configurations of ALMA, resulting in different synthesized beams to study five highly dense ($>10^7$ cm^{-3}) prestellar cores in the Orion molecular cloud. We found that in addition to detection using the ALMA-ACA-configuration (6″), these cores are also detected using the ALMA-TM2-configuration (1.2″) which implies that the cores have a centrally dense region of size ∼2000 au. No NIR/MIR emission has been detected toward these cores, signifying that the cores are starless/prestellar in nature. The cores are found to be gravitationally unstable, and at the onset of star formation we found two substructures of sizes ranging from 800–1700 au and masses >0.08–0.84 $M_\odot$ toward the core G205-M3. Considering that the freefall time is shorter than the coalescence time of the substructures, and they are likely bound within a separation of ∼1200 au, we speculate that this core will produce a wide binary or multiple star system.

This paper makes use of the following ALMA data: ADS/JAO.ALMA#2018.1.00302.S. ALMA is a partnership of ESO (representing its member states), NSF (USA) and NINS (Japan), together with NRC (Canada), MOST and ASIAA (Taiwan), and KASI (Republic of Korea), in cooperation with the Republic of Chile. The Joint ALMA Observatory is operated by ESO, auI/NRAO, and NAOJ. We thank the reviewer for helpful comments and suggestions. D.S. and S.Y. L. acknowledge support from the Ministry of Science and Technology (MoST) with grants 108-2112-M-001-048- and 108-2112-M-001-052-. T.L. acknowledges the support from the international partnership program of the Chinese Academy of Sciences through grant No.114231KYSB20200009, National Natural Science Foundation of China (NSFC) through grant NSFC No.12073061, and Shanghai Pujiang Program 20PJ1415500. N.H. acknowledges MoST 108-2112-M-001-017 and MoST 109-2112-M-001-023 grants. G.G. acknowledges support from ANID project AFB 170002. L.B. acknowledges support from ANID project AFB-170002. S.L.Q. is supported by the National Natural Science Foundation of China under grant No. U1631237. D.J. is supported by NRC Canada and by an NSERC Discovery Grant. V.M.P. acknowledges support by the Spanish MINECO under project AYA2017-88754-P, and financial support from the State Agency for Research of the Spanish Ministry of Science and Innovation through the "Unit of Excellence María de Maeztu 2020-2023" award to the Institute of Cosmos Sciences (CEX2019-000918-M). C.W.L. is supported by the Basic Science Research Program through the National Research Foundation of Korea (NRF) funded by the Ministry of Education, Science and Technology (NRF-2019R1A2C1010851). A.S. acknowledges financial support from the NSF through grant AST-1715876. The research was carried out in part at the Jet Propulsion Laboratory, which is operated for NASA by the California Institute of Technology. D. L. acknowledges support from NSFC No. 11911530226 and 11725313. K.T. was supported by JSPS KAKENHI grant No. 20H05645. J.H. thanks the NSFC grant No. 11873086 and Yunnan Province of China (No. 2017HC018).This work is sponsored (in part) by the Chinese Academy of Sciences (CAS), through a grant to the CAS South America Center for Astronomy (CASSACA) in Santiago, Chile.

Appendix
Dendrogram Analysis

In addition to visual identification of substructures toward the prestellar core G205-M3 (see Figure 2(d)), we also show the identification of the substructures with the dendrogram analysis, which is often employed in identifying and labeling clumpy structures (Rosolowsky et al. 2008; Pineda et al. 2015). We ran the dendrogram algorithm with min_value = 4σ (minimum intensity considered in the analysis) and min_delta = 2σ (minimum spacing between isocontours). Two substructures are clearly identified and presented in Figure 4 (red contours). The separation between the blobs, B1 and B2 as obtained from the dendrogram analysis, based on the peak position of the blobs is 1148 au. If we consider the position of the peaks of B1 and B2 as obtained from Gaussian fittings (presented in Table 1) then the separation is given by 1360 ± 140 au, considering the fitting uncertainties. So, in general, we consider the separation ∼1200 au, as mentioned in the text.

The image presented in Figure 4 corresponds to the combined data of ALMA (ACA, TM2 and TM1 configurations) with a uv-taper of 150 kλ ($\sim$0.″8). The dust emission of the five dense prestellar cores, which were detected in ALMA-TM2 ($\sim$1.″2), resolved out at the highest observing resolution (ALMA-TM1; $\sim$0.″3). So, to identify the substructures from the dust continuum images, we applied a range of uv-tapering on the combined ALMA data from 100 kλ to 200 kλ (which corresponds to resolution from 0.″6 to 1.″0). The substructures of G205.46-14.56M3 appear most prominent in ALMA combined data at $\sim$0.″8–1.″0 resolution (with uv-taper of 100–150 kλ), but at higher resolutions (beyond 200 kλ) their emission was resolved out.

ORCID iDs

Dipen Sahu https://orcid.org/0000-0002-4393-3463
Sheng-Yuan Liu https://orcid.org/0000-0003-4603-7119
Tie Liu https://orcid.org/0000-0002-5286-2564
Neal J. Evans II https://orcid.org/0000-0001-5175-1777
Naomi Hirano https://orcid.org/0000-0001-9304-7884
Ken'ichi Tatematsu https://orcid.org/0000-0002-8149-8546
Chin-Fei Lee https://orcid.org/0000-0002-3024-5864
Kee-Tae Kim https://orcid.org/0000-0003-2412-7092
Somnath Dutta https://orcid.org/0000-0002-2338-4583
Leonardo Bronfman https://orcid.org/0000-0002-9574-8454
Maria Cunningham https://orcid.org/0000-0001-7020-6176
David J. Eden https://orcid.org/0000-0002-5881-3229
Paul F. Goldsmith https://orcid.org/0000-0002-6622-8396
Jinhua He https://orcid.org/0000-0002-3938-4393
Shih-Ying Hsu https://orcid.org/0000-0002-1369-1563
Kai-Syun Jhan https://orcid.org/0000-0003-2069-1403
Doug Johnstone https://orcid.org/0000-0002-6773-459X
Mika Juvela https://orcid.org/0000-0002-5809-4834
Gwanjeong Kim https://orcid.org/0000-0003-2011-8172
Yi-Jehng Kuan https://orcid.org/0000-0002-4336-0730
Woojin Kwon https://orcid.org/0000-0003-4022-4132
Chang Won Lee https://orcid.org/0000-0002-3179-6334
Jeong-Eun Lee https://orcid.org/0000-0003-3119-2087
Di Li https://orcid.org/0000-0003-3010-7661
Pak Shing Li https://orcid.org/0000-0001-8077-7095
Shanghuo Li https://orcid.org/0000-0003-1275-5251
Veli-Matti Pelkonen https://orcid.org/0000-0002-8898-1047
Patricio Sanhueza https://orcid.org/0000-0002-7125-7685
Hsien Shang https://orcid.org/0000-0001-8385-9838
Archana Soam https://orcid.org/0000-0002-6386-2906
Yuefang Wu https://orcid.org/0000-0002-5076-7520
Qizhou Zhang https://orcid.org/0000-0003-2384-6589
Jianjun Zhou https://orcid.org/0000-0003-0356-818X

References

André, P., Di Francesco, J., Ward-Thompson, D., et al. 2014, in Protostars and Planets VI, ed. H. Beuther et al. (Tucson, AZ: Univ. Arizona Press), 27
Bonnor, W. B. 1956, MNRAS, 116, 351
Caselli, P. 2011, in IAU Symp. 280, The Molecular Universe, ed. J. Cernicharo & R. Bachiller (Cambridge: Cambridge Univ. Press), 19
Caselli, P., Pineda, J. E., Zhao, B., et al. 2019, ApJ, 874, 89
Cesaroni, R., & Wilson, T. L. 1994, A&A, 281, 209
Chen, X., & Arce, H. G. 2010, ApJL, 720, L169
Chen, X., Arce, H. G., Zhang, Q., et al. 2013, ApJ, 768, 110
Crapsi, A., Caselli, P., Walmsley, M. C., & Tafalla, M. 2007, A&A, 470, 221
Dunham, M. M., Offner, S. S. R., Pineda, J. E., et al. 2016, ApJ, 823, 160
Dutta, S., Lee, C.-F., Liu, T., et al. 2020, ApJS, 251, 20
Ebert, R. 1955, ZAp, 37, 217
Fisher, R. T. 2004, ApJ, 600, 769
Friesen, R. K., Di Francesco, J., Bourke, T. L., et al. 2014, ApJ, 797, 27
Goodwin, S. P., Whitworth, A. P., & Ward-Thompson, D. 2004, A&A, 423, 169
Hsu, S.-Y., Liu, S.-Y., Liu, T., et al. 2020, ApJ, 898, 107
Karnath, N., Megeath, S. T., Tobin, J. J., et al. 2020, ApJ, 890, 129
Kauffmann, J., Bertoldi, F., Bourke, T. L., Evans, N. J., I., & Lee, C. W. 2008, A&A, 487, 993
Kauffmann, J., Pillai, T., & Goldsmith, P. F. 2013, ApJ, 779, 185
Keto, E., & Caselli, P. 2010, MNRAS, 402, 1625
Kim, G., Tatematsu, K., Liu, T., et al. 2020, ApJS, 249, 33
Kirk, H., Johnstone, D., Di Francesco, J., et al. 2016, ApJ, 821, 98
Kirk, H., Dunham, M. M., Francesco, J. D., et al. 2017, ApJ, 838, 114
Kirk, J. M., Crutcher, R. M., & Ward-Thompson, D. 2009, ApJ, 701, 1044
Kounkel, M., Covey, K., Suárez, G., et al. 2018, AJ, 156, 84
McMullin, J. P., Waters, B., Schiebel, D., Young, W., & Golap, K. 2007, in ASP Conf. Ser. 376, Astronomical Data Analysis Software and Systems XVI, ed. R. A. Shaw, F. Hill, & D. J. Bell (San Francisco, CA: ASP), 127
Megeath, S. T., Gutermuth, R., Muzerolle, J., et al. 2012, AJ, 144, 192
Nakamura, F., Takakuwa, S., & Kawabe, R. 2012, ApJL, 758, L25
Offner, S. S. R., Capodilupo, J., Schnee, S., & Goodman, A. A. 2012, MNRAS, 420, L53
Offner, S. S. R., Kratter, K. M., Matzner, C. D., Krumholz, M. R., & Klein, R. I. 2010, ApJ, 725, 1485
Ohashi, S., Sanhueza, P., Sakai, N., et al. 2018, ApJ, 856, 147
Ossenkopf, V., & Henning, T. 1994, A&A, 291, 943
Padoan, P., & Nordlund, Å. 2002, ApJ, 576, 870
Palau, A., Zapata, L. A., Román-Zúñiga, C. G., et al. 2018, ApJ, 855, 24
Pineda, J. E., Offner, S. S. R., Parker, R. J., et al. 2015, Natur, 518, 213
Rosolowsky, E. W., Pineda, J. E., Kauffmann, J., & Goodman, A. A. 2008, ApJ, 679, 1338
Schnee, S., Enoch, M., Johnstone, D., et al. 2010, ApJ, 718, 306
Schnee, S., Sadavoy, S., Di Francesco, J., Johnstone, D., & Wei, L. 2012, ApJ, 755, 178
Shirley, Y. L., Evans, N. J., Neal, J., I., Rawlings, J. M. C., & Gregersen, E. M. 2000, ApJS, 131, 249
Stutz, A. M., Tobin, J. J., Stanke, T., et al. 2013, ApJ, 767, 36
Takahashi, S., Ho, P. T. P., Teixeira, P. S., Zapata, L. A., & Su, Y.-N. 2013, ApJ, 763, 57
Tatematsu, K., Liu, T., Kim, G., et al. 2020, ApJ, 895, 119
Tobin, J. J., Kratter, K. M., Persson, M. V., et al. 2016, Natur, 538, 483
Tokuda, K., Fujishiro, K., Tachihara, K., et al. 2020, arXiv:2006.06361
Ward-Thompson, D., Motte, F., & Andre, P. 1999, MNRAS, 305, 143
Ward-Thompson, D., Scott, P. F., Hills, R. E., & Andre, P. 1994, MNRAS, 268, 276
Yi, H.-W., Lee, J.-E., Liu, T., et al. 2018, ApJS, 236, 51